TECHNICAL UNIVERSITY OF LIBEREC
Faculty of Mechatronics, Informatics
and Interdisciplinary Studies

Large-Eddy Simulations for Aeroacoustics of Human Phonation

Dissertation thesis summary

Study programme: P3901 – Applied Sciences in Engineering
Study branch: 3901V055 – Applied Sciences in Engineering

Author: **Ing. Martin Lasota**
Supervisor: doc. Ing. Petr Šidlof, Ph.D.

Liberec 2022

Abstrakt (CZ)
Disertační práce se zabývá numerickým modelováním 3D nestlačitelného proudění vzduchu při lidské fonaci pěti kardinálních samohlásek /u, i, ɑ, o, æ/. Vědecký přínos této práce je v popisu souvislosti mezi výpočtem turbulentního proudění při použití konvenčního subgrid modelu (jednorovnicový, WALE), či nově implementovaného anizotropního minimálně disipačního (AMD) subgrid modelu a jeho vlivu na aeroakustický výpočet fonace. Vzhledem k velké škále měřítek v turbulentním proudění a v akustice je simulace rozdělena tak, že výpočet nestlačitelného proudění v hrtanu je realizován metodou konečných objemů na jemné síti a zdroje zvuku včetně šíření zvukových vln od hrtanu až do vyzařovaného prostoru okolo úst metodou konečných prvků na hrubé akustické síti.

Abstract
This dissertation deals with numerical modeling of 3D incompressible laryngeal flow during human phonation of five cardinal vowels /u, i, ɑ, o, æ/. This work aims to describe the correlation between turbulent flow simulations with a conventional (One-equation, WALE) or newly implemented anisotropic minimum dissipation (AMD) subgrid-scale model and its impact on the aeroacoustic spectrum in human phonation. Given the large variety of scales in the flow and acoustics, the simulation is separated in two steps: computing the flow in the larynx using the finite volume method on a fine grid followed by computing the sound sources and wave propagation from the larynx to the radiation space around the mouth using the finite element method on a coarse acoustic grid.

Klíčová slova (CZ)
simulace pohybu velkých vírů; subgrid model; anizotropní minimálně disipační model; perturbovaná konvektivní vlnová rovnice; modelování lidské fonace;

Keywords
large-eddy simulation; subgrid-scale model; anisotropic minimum dissipation model; perturbed convective wave equation; human phonation modelling;

Contents

1 Introduction

1.1 Principles of voice production

The generation of a human voice is a highly complex biophysical process, where the viscoelastic multi-layered tissues of the vocal folds interact with the airflow expired from the lungs, start to self-oscillate, and close the channel periodically. The vocal fold oscillation and glottal closure modulate the mass flux, create complex turbulent structures and pressure disturbances, which form the voice source. This source signal is modulated by the vocal tract, radiated from the mouth, and perceived as a human voice. Physiological principles are precisely described in the monograph by Titze (1994).

1.2 Objectives of the thesis

This thesis builds on the work of the author's predecessors (Šidlof et al., 2015; Zörner et al., 2016). The main objectives of the thesis are as follows:

- To perform 3D large-eddy simulations of laryngeal airflow.
- To perform 3D aeroacoustic simulations of human phonation.
- To perform deep literature search and seek for recent less common subgrid-scale turbulence models, potentially suitable for laryngeal flow modeling.
- To implement such a new subgrid-scale model in OpenFOAM.
- To make a conclusion about the impact of using subgrid-scale turbulence models on human phonation modelling.

The full version of the doctoral thesis is available here:
https://astra.nti.tul.cz/~martin.lasota/Lasota-PhD2022.pdf

2 CFD model of incompressible laryngeal flow

2.1 Mathematical model

Large-eddy simulation is a mathematical concept for modeling turbulent flows, which deals with flow structures carrying most kinetic energy, i.e. spatially organized large scales. These consist of two main categories: coherent structures and coherent vortices of recognizable shape (Lesieur et al., 2005). In the numerical implementation, the characteristic length Δ, defining a cutoff between resolved large scales and modeled subgrid scales, is usually given by the mesh grid spacing (Versteeg and Malalasekera, 2007).

In the LES concept, any flow variable $f(\mathbf{x},t)$, where $\mathbf{x} = (x_1, x_2, x_3)$ is the spatial coordinate and t time, may be decomposed as

$$f(\mathbf{x},t) = \overline{f}(\mathbf{x},t) + f'(\mathbf{x},t), \tag{2.1}$$

where $\overline{f}(\mathbf{x},t) = G_f(\mathbf{x}) * f(\mathbf{x},t) = \int G_f(\mathbf{r},\mathbf{x},\Delta) f(\mathbf{x}-\mathbf{r},t)\mathrm{d}\mathbf{r}$ is the large-scale component, obtained by spatial filtering, and $f'(x,t)$ is the small subgrid-scale contribution. Filtered variables for LES are functions of time and space, unlike the Reynolds averaged variables, hence in LES: $\overline{\overline{f}} \neq \overline{f}$, $\overline{f'} \neq 0$.

The convolution introduced above contains a filter function G_f separating spatial scales. Commonly used filters are the top-hat filter (2.2), the Gaussian filter (2.3) and the spectral cut-off filter (2.4):

$$G_f(\mathbf{r},\mathbf{x},\Delta) = \begin{cases} 1/\Delta^3 & \text{for } |\mathbf{r}| \leq \Delta/2, \\ 0 & \text{otherwise,} \end{cases} \tag{2.2}$$

$$G_f(\mathbf{r},\mathbf{x},\Delta) = \Big(\frac{6}{\pi\Delta^2}\Big)^{1/2} \exp\Big(-\frac{6|\mathbf{r}|^2}{\Delta^2}\Big), \tag{2.3}$$

$$G_f(\mathbf{r},\mathbf{x},\Delta) = \prod_{i=1}^{3} \frac{\sin(r_i/\Delta)}{r_i}. \tag{2.4}$$

The top-hat filter is used in the current simulation, which is a common choice in low-order finite volume methods.

The effect of subgrid-scale (SGS) contributions on the large flow scales relies on the assumption of isotropic (non-directional) small-scale turbulence and is modeled. Compared to the Reynolds stresses in RANS, the SGS stresses carry much less of the turbulent energy, so the model's accuracy is less critical. The LES solution seeks to compute only the scales of motion larger or equal than the filter width Δ.

The continuity and momentum equations for the incompressible fluid flow, with LES filtering applied, can be written as

$$\frac{\partial \overline{u}_i}{\partial x_i} = 0, \tag{2.5}$$

$$\frac{\partial \overline{u}_i}{\partial t} + \frac{\partial}{\partial x_j}(\overline{u_i u_j}) = -\frac{1}{\rho}\frac{\partial \overline{p}}{\partial x_i} + \nu \frac{\partial^2 \overline{u}_i}{\partial x_j \partial x_j}, \tag{2.6}$$

where $\overline{u}_i$ is the filtered velocity, $\overline{p}$ represents the filtered static pressure and ν is the kinematic molecular viscosity. The term $\overline{u_i u_j}$ is the dyadic product and cannot be expressed directly (Ferziger, 1998). Modification of the momentum equation (2.6) by $+\frac{\partial}{\partial x_j}(\overline{u}_i \overline{u}_j)$ yields

$$\frac{\partial \overline{u}_i}{\partial t} + \frac{\partial}{\partial x_j}(\overline{u}_i \overline{u}_j) = -\frac{1}{\rho}\frac{\partial \overline{p}}{\partial x_i} + \nu \frac{\partial^2 \overline{u}_i}{\partial x_j \partial x_j} - \frac{\partial \tau_{ij}}{\partial x_j}. \tag{2.7}$$

The new term on the right-hand side of (2.7) is the divergence of the subgrid-scale (SGS) turbulent stress tensor

$$\tau_{ij} = \overline{u_i u_j} - \overline{u}_i \overline{u}_j = -(\overline{u_i' u_j'} + \overline{\overline{u}_i u_j'} + \overline{u_i' \overline{u}_j} + \overline{\overline{u}_i \overline{u}_j} - \overline{u}_i \overline{u}_j), \tag{2.8}$$

where the individual tensors are: $-\overline{u_i' u_j'}$ the Reynolds-stress-like term, $-(\overline{\overline{u}_i u_j'} + \overline{u_i' \overline{u}_j})$ the Clark term (Clark et al., 1979) and $-(\overline{\overline{u}_i\ \overline{u}_j} + \overline{u}_i \overline{u}_j)$ the Leonard term (Leonard, 1975). The SGS stress tensor τ_{ij} is left to be modeled to close the set of equations.

Since the turbulence is not fully understood, a wide range of closure models have been introduced, often using heuristic and ad hoc techniques.

2.1.1 AMD SGS model

The anisotropic minimum-dissipation (AMD) subgrid-scale model was derived by Rozema et al. (2015) with modified Poincaré inequality addressing the grid anisotropy. The AMD model has not yet been applied in numerical simulation of human phonation, and thus the model was chosen as a candidate to new implementation performed by the author of this thesis into the OpenFOAM CFD package.

AMD is developed from the QR model (Verstappen, 2011), and both models are in the category "minimum-dissipation models". The main objective of these models is to ensure that the energy of subgrid scales is not increasing

$$\partial_t \int_{\Omega_\delta} \frac{1}{2} u_i' u_i' \mathrm{d}x \leq 0. \tag{2.9}$$

In the situation where subgrid scales are assumed to be periodical on filter box Ω_δ, it is possible to apply the Poincaré inequality, and define thus the upper bound of the SGS energy on the left side

$$\int_{\Omega_\delta} \frac{1}{2} u_i' u_i' \mathrm{d}x \leq C_A \int_{\Omega_\delta} \frac{1}{2} (\partial_i u_j)(\partial_i u_j) \mathrm{d}x. \tag{2.10}$$

The right hand side corresponds to the velocity gradient energy, and C_A is the Poincaré constant

$$C_A = (\delta/\pi)^2 \tag{2.11}$$

for the LES filter of width δ. The evolution of the right hand side in (2.10) can be written, considering Taylor expansion of the exact subgrid-scale tensor, as

$$\partial_t\left(\frac{1}{2}(\partial_i u_j)(\partial_i u_j)\right) = \overbrace{-(\partial_k u_i)(\partial_k u_j)S_{ij}}^{R1} - (\partial_k S_{ij})\partial_k(2\nu S_{ij}) - (\partial_k S_{ij})\partial_k(2\nu_t^{QR} S_{ij}) + \partial_i f_i \tag{2.12}$$

where f_i is the flux of velocity gradient energy and ν_t^{QR} is the turbulent viscosity defined by the QR model. Upon spatial integration over the LES filter, the divergence term $\partial_i f_i$ can be rewritten to a boundary integral. The boundary integrals express transport of velocity gradient energy instead of production or dissipation and thus can be ignored in the derivation of minimum-dissipation models (Rozema et al., 2015). The term $R1$ from (2.12) is the production of the velocity gradient energy and can be rewritten to

$$-(\partial_k u_i)(\partial_k u_j)S_{ij} = 4III_{\mathbb{S}} + \boldsymbol{\nabla}\cdot(...), \tag{2.13}$$

having the important third invariant of the resolved strain-rate tensor

$$III_{\mathbb{S}} = -\det\mathbb{S} = -\frac{1}{3}\mathrm{tr}(\mathbb{S}^3) = -\frac{1}{3}S_{ij}S_{jk}S_{ki}. \tag{2.14}$$

The dissipation rate of the velocity gradient energy is

$$\int_{\Omega_\delta} 2II_{\mathbb{S}}\ \mathrm{d}x = \int_{\Omega_\delta} S_{ij}S_{ij}\mathrm{d}x \leq C_\delta \int_{\Omega_\delta} (\partial_k S_{ij})(\partial_k S_{ij})\mathrm{d}x, \tag{2.15}$$

where the second invariant is

$$II_{\mathbb{S}} = \frac{1}{2}\mathrm{tr}(\mathbb{S}^2) = \frac{1}{2}S_{ij}S_{ij}. \tag{2.16}$$

Finally, the condition which is necessary for the eddy disipation to stop the production of the velocity gradient energy is in the form

$$4\int_{\Omega_\delta} III_{\mathbb{S}}\ \mathrm{d}x \leq 4\frac{\nu_t^{QR}}{C_A}\int_{\Omega_\delta} II_{\mathbb{S}}\ \mathrm{d}x. \tag{2.17}$$

The minimum eddy dissipation is thus equal to

$$\nu_t^{QR} = C_A\delta^2\frac{\max\{III_{\mathbb{S}}, 0\}}{II_{\mathbb{S}}}, \tag{2.18}$$

where C_A is a model constant. The third invariant $III_{\mathbb{S}}$ vanishes in flows that are laminar (Vreman, 2004). To summarize:

- The production term in (2.12) is proportional to the dissipation of the leading term on the right-hand side in (2.13).
- The dissipation of the energy of subgrid-scales is proportional to $III_{\mathbb{S}}$.
- The QR model is consistent with the eddy dissipation of the exact subgrid-scale tensor.

The main drawback of the QR model is necessity to set a filter width δ and applicability on isotropic grids only.

The AMD model can sidestep the dependence of model constants on the filter width by using the modified Poincaré inequality

$$\int_{\Omega_\delta} \frac{1}{2} u_i' u_i' \mathrm{d}x \leq C_A \int_{\Omega_\delta} \overbrace{\frac{1}{2} (\underbrace{\delta x_i \partial_i}_{R3} u_j)(\delta x_i \partial_i u_j)}^{R2} \mathrm{d}x, \tag{2.19}$$

where Ω_δ is the filter box, having dimensions δx_1, δx_2 and δx_3, and C_A is a model constant, which will be discussed later. The term $R2$ is the scaled velocity gradient energy, $R3$ the scaled gradient operator. The inequality (2.19) demonstrates that the sub-grid energy is confined by imposing a bound on the term $R2$ (Rozema et al., 2015). Time derivative is applied on the term $R2$ and the evolution equation of $R2$ on the filter box δx_i is expressed

$$\begin{aligned} \partial_t \left(\frac{1}{2} (\delta x_i \partial_i u_j)(\delta x_i \partial_i u_j \right) = & \overbrace{-(\delta x_k \partial_k u_i)(\delta x_k \partial_k u_j) S_{ij}}^{R4} - \\ & - (\nu + \nu_t^A) \delta x_k \partial_k (\partial_i u_j) \delta x_k \partial_k (\partial_i u_j) + \partial_i f_i, \end{aligned} \tag{2.20}$$

where the term $R4$ is the production of the scaled velocity gradient energy. This means the third invariant is not computed from the resolved strain-rate tensor S_{ij}, such as in the QR model (2.14), and for the second invariant in (2.16).

The following inequality ensures that the AMD model predicts sufficient dissipation to stop the production of scaled velocity gradient energy $R4$

$$\int_{\Omega_\delta} -(\delta x_k \partial_k u_i)(\delta x_k \partial_k u_j) S_{ij} \mathrm{d}x \leq \frac{\nu_t^A}{C_A} \int_{\Omega_\delta} (\partial_i u_j)(\partial_i u_j) \mathrm{d}x, \tag{2.21}$$

where the minimum dissipation effect is held by satisfying

$$\nu_t^A = C_A \frac{\max\{\int_{\Omega_\delta} -(\delta x_k \partial_k u_i)(\delta x_k \partial_k u_j) S_{ij} \mathrm{d}x, 0\}}{\int_{\Omega_\delta} (\partial_l u_m)(\partial_l u_m) \mathrm{d}x}. \tag{2.22}$$

Integrals in (2.22) can be approximated by the mid-point rule, and the turbulent viscosity from AMD ν_t^A results in a more practical form

$$\nu_t^A = C_A \frac{\overbrace{\max\{\overbrace{-(\delta x_k \partial_k u_i)(\delta x_k \partial_k u_j) S_{ij}}^{-A_{ij} S_{ij}}, 0\}}^{n_-}}{\underbrace{(\partial_l u_m)(\partial_l u_m)}_{d_-}}. \tag{2.23}$$

The terms $-A_{ij} S_{ij}$ and d_- are written as

$$
\begin{aligned}
A_{ij}S_{ij} &= (\delta x_k \partial_k u_i)(\delta x_k \partial_k u_j) S_{ij} = \\
&= \sum_{i,j=1}^{3} \left(\delta x_1 \frac{\partial u_i}{\partial x_1} + \delta x_2 \frac{\partial u_i}{\partial x_2} + \delta x_3 \frac{\partial u_i}{\partial x_3}\right)\left(\delta x_1 \frac{\partial u_i}{\partial x_1} + \delta x_2 \frac{\partial u_i}{\partial x_2} + \delta x_3 \frac{\partial u_i}{\partial x_3}\right) S_{ij} = \\
&= S_{11}\left(\delta x_1 \frac{\partial u_1}{\partial x_1} + \delta x_2 \frac{\partial u_1}{\partial x_2} + \delta x_3 \frac{\partial u_1}{\partial x_3}\right)\left(\delta x_1 \frac{\partial u_1}{\partial x_1} + \delta x_2 \frac{\partial u_1}{\partial x_2} + \delta x_3 \frac{\partial u_1}{\partial x_3}\right) + \\
&+ S_{12}\left(\delta x_1 \frac{\partial u_1}{\partial x_1} + \delta x_2 \frac{\partial u_1}{\partial x_2} + \delta x_3 \frac{\partial u_1}{\partial x_3}\right)\left(\delta x_1 \frac{\partial u_2}{\partial x_1} + \delta x_2 \frac{\partial u_2}{\partial x_2} + \delta x_3 \frac{\partial u_2}{\partial x_3}\right) + \\
&+ S_{13}\left(\delta x_1 \frac{\partial u_1}{\partial x_1} + \delta x_2 \frac{\partial u_1}{\partial x_2} + \delta x_3 \frac{\partial u_1}{\partial x_3}\right)\left(\delta x_1 \frac{\partial u_3}{\partial x_1} + \delta x_2 \frac{\partial u_3}{\partial x_2} + \delta x_3 \frac{\partial u_3}{\partial x_3}\right) + \\
&+ S_{21}\left(\delta x_1 \frac{\partial u_2}{\partial x_1} + \delta x_2 \frac{\partial u_2}{\partial x_2} + \delta x_3 \frac{\partial u_2}{\partial x_3}\right)\left(\delta x_1 \frac{\partial u_1}{\partial x_1} + \delta x_2 \frac{\partial u_1}{\partial x_2} + \delta x_3 \frac{\partial u_1}{\partial x_3}\right) + \\
&+ S_{22}\left(\delta x_1 \frac{\partial u_2}{\partial x_1} + \delta x_2 \frac{\partial u_2}{\partial x_2} + \delta x_3 \frac{\partial u_2}{\partial x_3}\right)\left(\delta x_1 \frac{\partial u_2}{\partial x_1} + \delta x_2 \frac{\partial u_2}{\partial x_2} + \delta x_3 \frac{\partial u_2}{\partial x_3}\right) + \\
&+ S_{23}\left(\delta x_1 \frac{\partial u_2}{\partial x_1} + \delta x_2 \frac{\partial u_2}{\partial x_2} + \delta x_3 \frac{\partial u_2}{\partial x_3}\right)\left(\delta x_1 \frac{\partial u_3}{\partial x_1} + \delta x_2 \frac{\partial u_3}{\partial x_2} + \delta x_3 \frac{\partial u_3}{\partial x_3}\right) + \\
&+ S_{31}\left(\delta x_1 \frac{\partial u_3}{\partial x_1} + \delta x_2 \frac{\partial u_3}{\partial x_2} + \delta x_3 \frac{\partial u_3}{\partial x_3}\right)\left(\delta x_1 \frac{\partial u_1}{\partial x_1} + \delta x_2 \frac{\partial u_1}{\partial x_2} + \delta x_3 \frac{\partial u_1}{\partial x_3}\right) + \\
&+ S_{32}\left(\delta x_1 \frac{\partial u_3}{\partial x_1} + \delta x_2 \frac{\partial u_3}{\partial x_2} + \delta x_3 \frac{\partial u_3}{\partial x_3}\right)\left(\delta x_1 \frac{\partial u_2}{\partial x_1} + \delta x_2 \frac{\partial u_2}{\partial x_2} + \delta x_3 \frac{\partial u_2}{\partial x_3}\right) + \\
&+ S_{33}\left(\delta x_1 \frac{\partial u_3}{\partial x_1} + \delta x_2 \frac{\partial u_3}{\partial x_2} + \delta x_3 \frac{\partial u_3}{\partial x_3}\right)\left(\delta x_1 \frac{\partial u_3}{\partial x_1} + \delta x_2 \frac{\partial u_3}{\partial x_2} + \delta x_3 \frac{\partial u_3}{\partial x_3}\right) \qquad (2.24)
\end{aligned}
$$

and

$$
\begin{aligned}
d_{-} &= (\partial_l u_m)(\partial_l u_m) = \\
&= \sum_{l,m=1}^{3} \left(\frac{\partial u_m}{\partial x_l}\right)\left(\frac{\partial u_m}{\partial x_l}\right) = \\
&= \left(\frac{\partial u_1}{\partial x_1}\right)\left(\frac{\partial u_1}{\partial x_1}\right) + \left(\frac{\partial u_2}{\partial x_1}\right)\left(\frac{\partial u_2}{\partial x_1}\right) + \left(\frac{\partial u_3}{\partial x_1}\right)\left(\frac{\partial u_3}{\partial x_1}\right) + \\
&+ \left(\frac{\partial u_1}{\partial x_2}\right)\left(\frac{\partial u_1}{\partial x_2}\right) + \left(\frac{\partial u_2}{\partial x_2}\right)\left(\frac{\partial u_2}{\partial x_2}\right) + \left(\frac{\partial u_3}{\partial x_2}\right)\left(\frac{\partial u_3}{\partial x_2}\right) + \\
&+ \left(\frac{\partial u_1}{\partial x_3}\right)\left(\frac{\partial u_1}{\partial x_3}\right) + \left(\frac{\partial u_2}{\partial x_3}\right)\left(\frac{\partial u_2}{\partial x_3}\right) + \left(\frac{\partial u_3}{\partial x_3}\right)\left(\frac{\partial u_3}{\partial x_3}\right) = \\
&= (\boldsymbol{\nabla}\mathbf{u}) : (\boldsymbol{\nabla}\mathbf{u}). \qquad (2.25)
\end{aligned}
$$

The implementation of $-A_{ij}S_{ij}$ is shown on lines 10 and 13, the whole nominator n_{-} is on line 13, and the whole denominator d_{-} refers to line 14; implemented into OpenFOAM (version 6 and 7).

```
1  template<class BasicTurbulenceModel>
2  void LAAMD<BasicTurbulenceModel>::correct()
3  {
4      LESeddyViscosity<BasicTurbulenceModel>::correct();
5
6      const volVectorField& U = this->U_;
7      tmp<volTensorField> tgradU(fvc::grad(U));
8      const volTensorField& gradU = tgradU();
9      volSymmTensorField S(dev(symm(gradU)));
10     volTensorField Aij= (this->delta()*gradU)&(this->delta()*(gradU).T());
11     dimensionedScalar my_null_("my_null_",
12         dimensionSet(0,2,-3,0,0,0,0), scalar(0));
13     volScalarField n_ = max(-Aij && S,my_null_);
14     volScalarField d_ = gradU && gradU;
15
16     //scalar C_A_ = 0.57735;
17     nu_amd_ = (0.57735*n_)/d_;
18
19     correctNut();
20 }
21
22 template<class BasicTurbulenceModel>
23 void LAAMD<BasicTurbulenceModel>::correctNut()
24 {
25     volScalarField k(this->k(fvc::grad(this->U_)));
26
27     this->nut_ =nu_amd_;
28     this->nut_.correctBoundaryConditions();
29     fv::options::New(this->mesh_).correct(this->nut_);
30
31     BasicTurbulenceModel::correctNut();
32 }
```

Line 17 shows the turbulent viscosity via computed by (2.23), including the value of the model constant C_A. The constant suitable for the AMD model is recommended from (Rozema et al., 2015) with respect to the order of discretization of Navier-Stokes equations, tested on decaying grid turbulence cases. The AMD model gave the best results with $C_A = 0.300$ for a central second-order scheme and $C_A = 0.212$ for a fourth-order scheme. A recent study by Zahiri and Roohi (2019) states an optimal value of the constant $C_A = \frac{1}{\sqrt{3}} = 0.577$ based on various study cases.

Rozema et al. (2015) has shown that after a Taylor expansion of τ_{ij} it can be shown that the AMD model is really consistent with the exact subgrid-scale stress tensor

$$\tau_{ij} = \overline{u_i u_j} - \overline{u}_i \overline{u}_j = \frac{1}{12}(\delta x_k \partial_k u_i)(\delta x_k \partial_k u_j) + \mathcal{O}(\delta x_i^4) \tag{2.26}$$

and the eddy dissipation of the exact subgrid-scale stress tensor is approximated as

$$-\tau_{ij} S_{ij} = -\frac{1}{12}(\delta x_k \partial_k u_i)(\delta x_k \partial_k u_j) S_{ij} + \mathcal{O}(\delta x_i^4), \tag{2.27}$$

which means that the term A_{ij} in (2.23) is consistent with the product of Taylor series in (2.27). The term A_{ij} is also referred as the gradient sub-filter model (Vreman, 1995). If the exact eddy dissipation gives zero dissipation, then the term A_{ij} as well, this means the

AMD model can be switched off for flows where the exact eddy dissipation is vanishing. Thus, the AMD model also switches off when no SGS energy is created (Rozema et al., 2015; Vreugdenhil and Taylor, 2018).

The anisotropic behavior of the AMD model can be advantageous in dynamic mesh applications, such as the moving grid within the glottis.

2.2 Geometry and boundary conditions

The computational domain for the CFD simulation represents a simplified model of the human larynx with a rectangular cross-section, consisting of a short subglottal channel, glottal constriction formed by the vocal folds, ventricles, further contraction by the false vocal folds, and straight supraglottal channel (see Fig. 2.1).

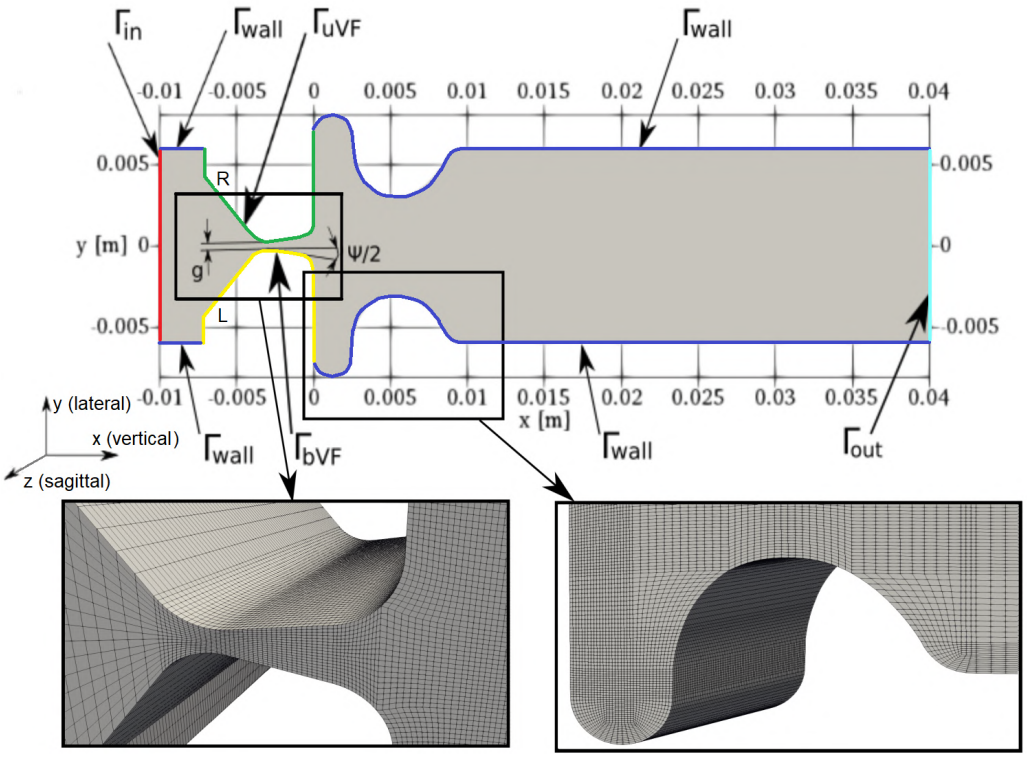

Fig. 2.1: Mid-coronal (x-y) section of the CFD computational domain, domain boundaries and details of the computational mesh. The z-normal (front and back) boundaries belong to Γ_{wall}. Enclosed figures about mesh representation are discussed in Chap. 2.3.

The geometry of vocal folds is based on the M5 parametric shape by Scherer et al. (2001). The false vocal folds were specified according to data published by Agarwal et al. (2003). The geometrical model is in 3D, having a square cross-section at inlet 12x12 mm. More details can be found in (Šidlof et al., 2015). The boundary conditions for the CFD model are summarized in Tab. 2.1. The flow is driven by constant pressure difference $P_k = \overline{p}/\rho = 300$ m^2/s^s between the inlet Γ_{in} and outlet Γ_{out}. The velocity on Γ_{in} and Γ_{out} is computed from the flux. The flow enters at the inlet and exits at the outlet or is set to

zero in case of backflow. On the fixed channel walls, a no-slip boundary condition $\mathbf{u} = \mathbf{0}$ is prescribed.

Tab. 2.1: Boundary conditions for the filtered flow velocity $\overline{\mathbf{u}}$ and static pressure $\overline{p}$. The symbol $\mathbf{n}$ is the unit outer normal and $h(\mathbf{x}, t)$ is the prescribed displacement of the vocal folds. Γ_{wall} also includes the front and back surface.

Boundary	$\overline{\mathbf{u}}$ [ms^{-1}]	$\overline{p}$ [Pa]
Γ_{in}	$\overline{\mathbf{u}} = \mathbf{0}$ if $\overline{\mathbf{u}} \cdot \mathbf{n} < 0$, $\nabla(\overline{\mathbf{u}}) \cdot \mathbf{n} = \mathbf{0}$ if $\overline{\mathbf{u}} \cdot \mathbf{n} > 0$	350
Γ_{out}	$\overline{\mathbf{u}} = \mathbf{0}$ if $\overline{\mathbf{u}} \cdot \mathbf{n} < 0$, $\nabla(\overline{\mathbf{u}}) \cdot \mathbf{n} = \mathbf{0}$ if $\overline{\mathbf{u}} \cdot \mathbf{n} > 0$	0
Γ_{bVF}, Γ_{uVF}	$\overline{u}_1 = 0$, $\overline{u}_2 = \frac{\partial}{\partial t} h(\mathbf{x}, t)$, $\overline{u}_3 = 0$	$\nabla(\overline{p}) \cdot \mathbf{n} = 0$
Γ_{wall}	$\overline{\mathbf{u}} = \mathbf{0}$	$\nabla(\overline{p}) \cdot \mathbf{n} = 0$

On the moving boundaries Γ_{bVF} and Γ_{uVF}, the flow velocity is equal to the velocity of the moving vocal fold surface, given by function $h(\mathbf{x}, t)$. The function $h(\mathbf{x}, t)$ based on the sinusoidal displacement $w_{1,2} = A_{1,2} \sin(2\pi f_o t + \xi_{1,2})$ ensures the vibrating motion of vocal folds in the medial-lateral (y) direction with two degrees of freedom. In the current simulation, the vocal folds oscillate symmetrically with a frequency $f_o = 100$ Hz, amplitudes at the superior and inferior vocal fold margin are $A_1 = A_2 = 0.3$ mm. The medial surface convergence angle is marked in Fig. 2.1 as $\psi/2$, which confines the convergent and divergent position (-10 deg and +10 deg). In this study, the oscillation of the vocal folds allows closing/opening the glottal gap g in the range 0.42-1.46 mm.

2.3 Mesh

In wall-bounded flows, the presence of solid walls fundamentally influences the flow dynamics, turbulence generation, and transport in the near-wall regions due to significant viscous stresses. The accuracy of the numerical simulation is thus closely related to the grid resolution near the walls.

The computational mesh in the current CFD simulation (see Fig. 2.1) is block-structured to capture well the boundary layer and consists of 2.1M hexahedral elements. An open source 3D finite volume mesh generator blockMesh was used to build the mesh. The mesh deforms in time due to vocal fold oscillation. The grid resolution in wall units was evaluated in three distinct time instants, corresponding to a maximum opening of the vocal folds, full closure during the divergent phase and full closure during the convergent phase. On the boundary Γ_{bVF} at the critical time when the vocal folds are maximally adducted were evaluated these values: $y^+_{avg} = 1.77$, $z^+ = 14$ and $x^+ = 8$.

2.4 Discretization and numerical solution

The Navier-Stokes equations were discretized using the collocated cell-centered Finite Volume Method. Fletcher (1991) demonstrated that even-ordered derivatives in the truncation error are associated with numerical dissipation, and odd-ordered spatial

derivatives are associated with the numerical dispersion in the solution. Ideally, LES simulations should use schemes with low numerical dissipation. The non-dissipative central differencing scheme, which was applied in this study, allows an accurate representation of the changing flow field (Launchbury, 2016). The discretization of the diffusion term is split into an orthogonal and cross-diffusion term, using a procedure described in (Jasak, 1996). Unlike the discretization of the temporal, convective, and orthogonal part of the diffusive term, the nonorthogonal correctors are treated explicitly.

CFD simulations were run in parallel on:

1. Charon (Metacentrum NGI - Faculty of Mechatronics, Technical University of Liberec)
   - 20 cores on a computational cluster, composed of nodes with two 10-core Intel Xeon Silver 4114 2.20GHz CPUs with 96GB RAM,
2. Fox (Computing center of the Czech Technical University in Prague)
   - 20 cores on a supercomputer (SGI Altix UV 100) with shared memory 576GB RAM with the involvement of 6-core Intel Xeon Nehalem 2.66GHz CPUs.

In order to have sufficient resolution in the spectrum of the aeroacoustic signal, a sufficiently long simulation time $t = 0.2$ s, i.e. 20 periods of vocal fold vibration, is needed. For such a setting, one CFD simulation required 27 - 37 days, i.e. about 15000 core-hours of computational time.

2.5 CFD results

The current study reports on the results of four CFD simulations using different turbulence modeling approaches, which are summarized in Tab. 2.2. The simulations were run in parallel on 20 CPU cores for 20 periods of vocal fold oscillations, either on the computational cluster Charon, or on the symmetric multiprocessing machine Fox.

Tab. 2.2: Overview of the CFD simulations.

Case	Type	SGS model	CPU	Cluster	Wall-time
LAM	laminar	-	20	Charon	27d 13h
OE	LES	One-Equation	20	Charon	34d 05h
WALE	LES	WALE	20	Charon	37d 13h
AMD	LES	AMD	20	Fox	34d 18h

2.5.1 Laryngeal flow rate

Fig. 2.2 shows the glottal opening and flow rates during the last four simulated cycles of vocal fold oscillation. The time t_N corresponds to the instant where the inferior margins of the vocal folds approach most and reduce the glottal opening to $5.58\,\mathrm{mm}^2$. Time instant t_C is the maximum approach of the superior vocal fold margins, where the glottal opening drops to $4.98\,\mathrm{mm}^2$. The third time instant, t_O, corresponds to the maximum glottal opening of $17.51\,\mathrm{mm}^2$. Glottal gaps listed in mm are in Tab. 2.3.
The subgrid-scale models affected the flow rates Q[l/s] (see Fig. 2.2): the predicted peak flow rate in the laminar case is higher than in the One-Equation, WALE and AMD

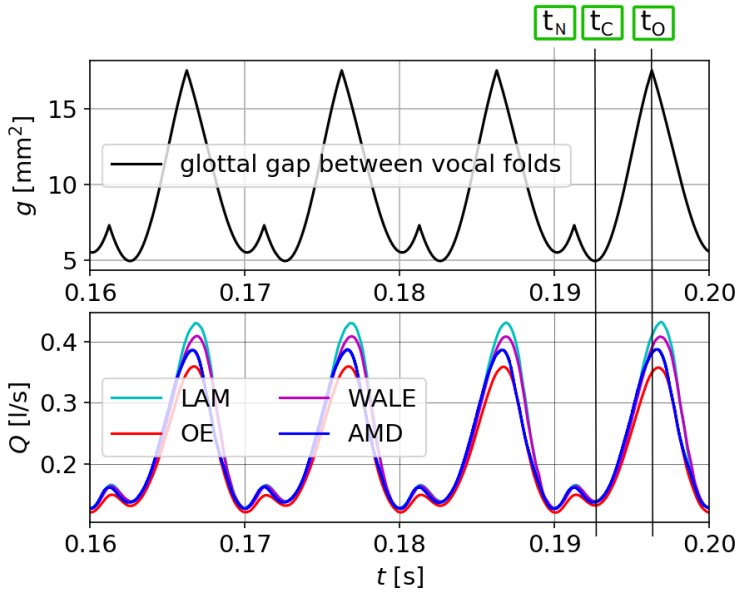

Fig. 2.2: Glottal gap and flow rates during four oscillation cycles. Time instants for further analysis: $t_{\mathrm{N}} = 0.1900$ s, $t_{\mathrm{C}} = 0.1927$ s and $t_{\mathrm{O}} = 0.1963$ s.

Tab. 2.3: Glottal gaps at time instants.

Time	g[mm^2]	VF gap[mm]
t_N	5.58	0.465
t_C	4.98	0.415
t_O	17.51	1.459

SGS models by 16.76%, 5.26% and 9.3%, respectively. This is caused by the different values of the SGS viscosity, which adds to the molecular viscosity and limits the flow rate through the glottal constriction. The laminar model does not capture the influence of small-scale turbulence, which corresponds to $\nu_t = 0$. The WALE SGS model and the One-Equation SGS model compute with non-zero SGS viscosity, with the latter one significantly higher due to the already mentioned deficiency of the One-Equation model, which overestimates the turbulent viscosity near the vocal fold surfaces. The flow rate does not reach zero value, corresponding physiologically to breathy phonation. The vocal folds do not fully close the glottal channel from technical reasons. The minimum flow rate is $Q_{min} \approx 0.122$ l/s. The maximum flow rates are between $0.358 - 0.434$ l/s, see Tab. 2.4. The peak flow rate predicted by the AMD model occurs sooner than in other simulations (when 66% of the VF cycle is reached).

Tab. 2.4: Minimum and maximum flow rates [l/s] and state of the oscillation cycle of vocal folds [%] when the maximum flow rate is reached.

Case	Q_{min}[l/s]	Q_{max}[l/s]	VF cycle(Q_{max})[%]
LAM	0.129	0.434	69
OE	0.122	0.358	67
WALE	0.128	0.409	69
AMD	0.127	0.389	66

2.5.2 Velocity and pressure distribution

The CFD simulations provide filtered velocity and pressure fields ($\overline{u}$, $\overline{p}$). For simplicity the overbars are dropped in the following presentation of results. Fig. 2.3 shows 3D laryngeal velocity fields during vocal fold oscillation. The jet in the supraglottal region interacts with turbulent structures and gradually decays.

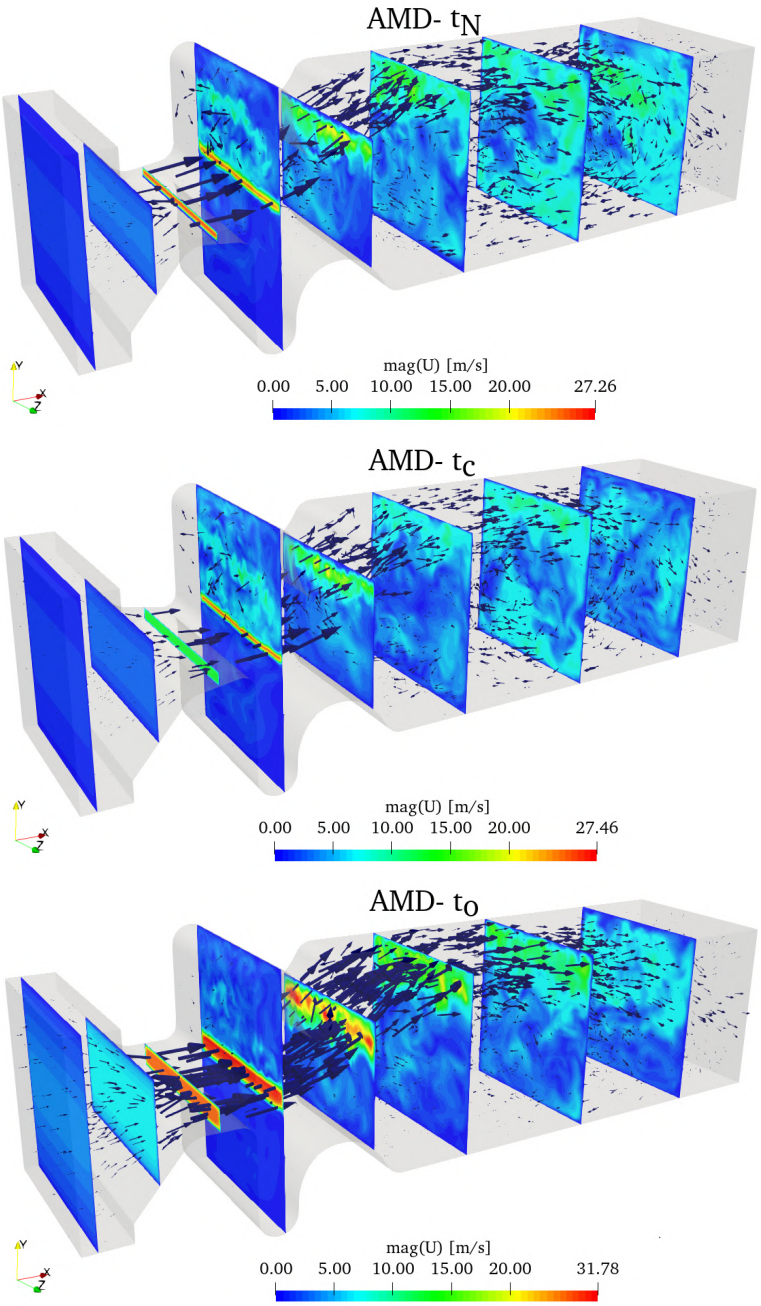

Fig. 2.3: Visualization of laryngeal flow at t_N, t_C and t_O. Contours of the jet can be observed.

2.5.3 Vorticity field

Vorticity ($\boldsymbol{\omega} = \nabla \times \mathbf{u}$) is commonly used for characterizing turbulence in cases with no entrainment rotation. The vorticity fields reveal the shear layers, where vortices are shed as a consequence of Kelvin-Helmholtz instability. The vortices may undergo successive instabilities, leading to a direct kinetic-energy cascade towards the small scales.

Fig. 2.4 shows vorticity fields presented in mid-coronal plane (x-y). The supraglottal jet deflects stochastically towards either of the ventricular folds. This behavior is not a consequence of the SGS model, it is caused by the bistability of the flow in this symmetric geometry (Erath and Plesniak, 2010; Lodermeyer et al., 2015). Detailed analysis of the vorticity within the glottal region shows that the average value of vorticity in glottal region is similar for all SGS models.

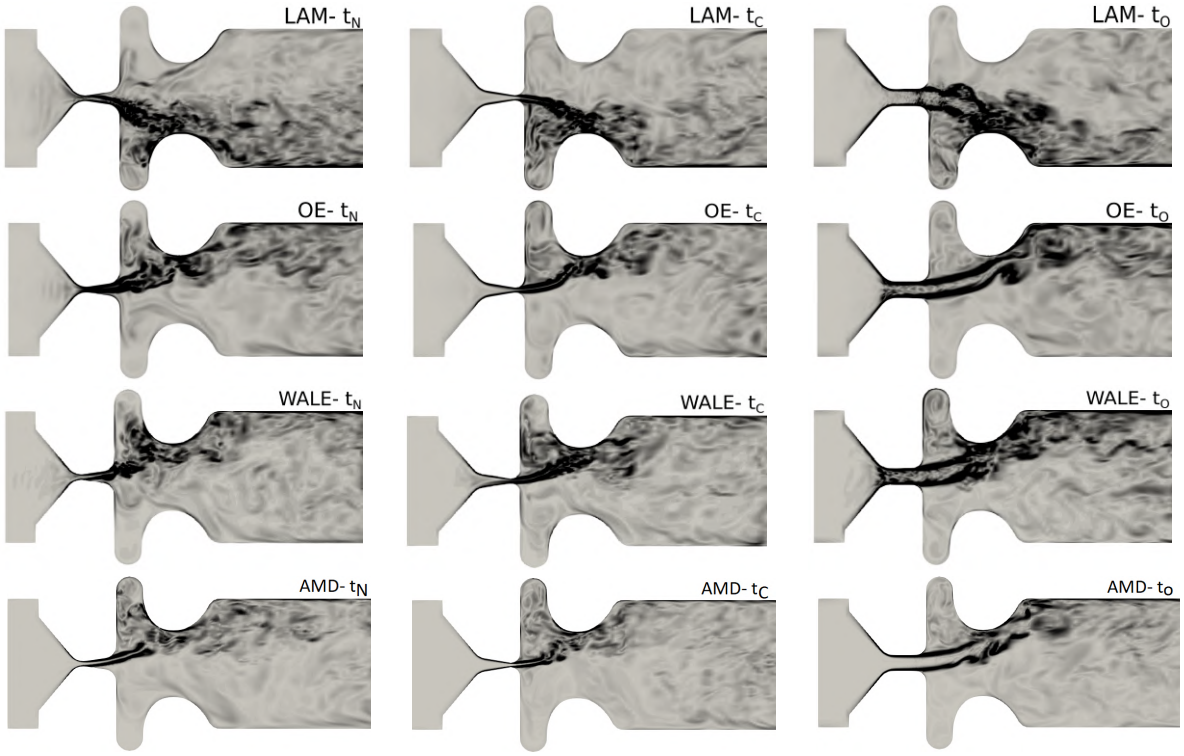

Fig. 2.4: Vorticity fields $|\boldsymbol{\omega}|$ in mid-coronal plane in range (0,30000) [s^{-1}].

Fig. 2.5 shows a complementary view on the magnitude of the vorticity vector $|\boldsymbol{\omega}|$ in mid-sagittal plane (x-z). The simulation with the AMD model predicts low vorticity in the vicinity of the glottis. The absence of vorticity may imitate the situation in the realistic larynx where the jet is frequently stopped and renewed, and thus the turbulent eddies are forced to be dissipated.

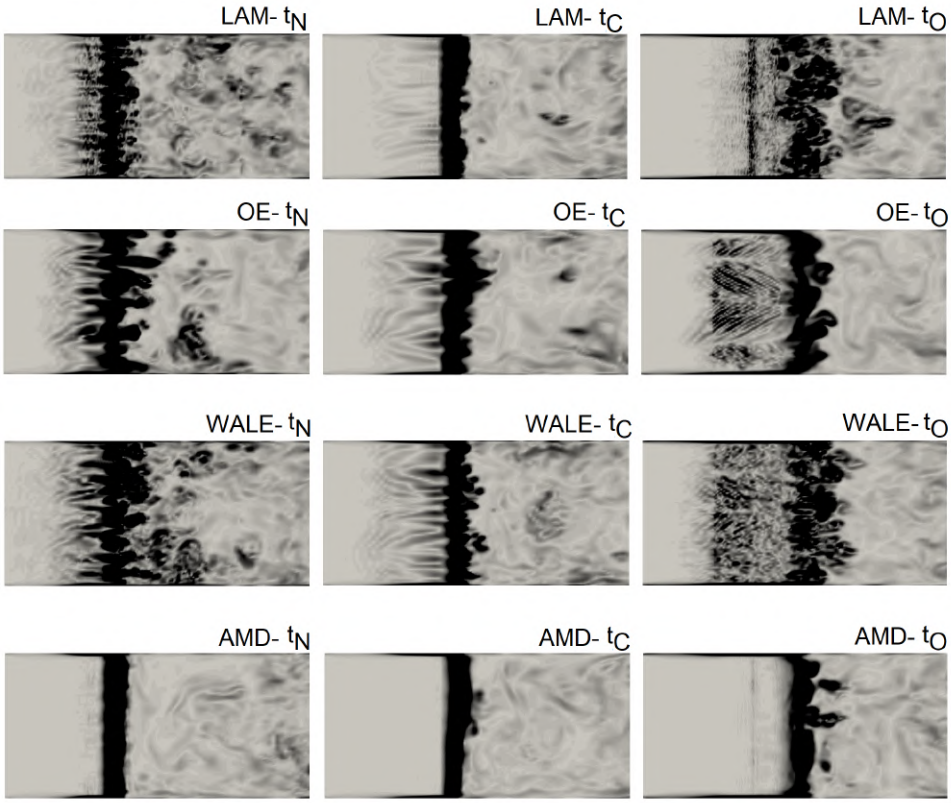

Fig. 2.5: Vorticity fields $|\boldsymbol{\omega}|$ in mid-sagittal plane in range (0,30000) [s^{-1}].

2.5.4 Turbulent viscosity field

The effect of the unresolved turbulent subgrid scales on the resolved scales is carried by the subgrid-scale turbulent viscosity ν_t.

Figs. 2.6-2.7 show that the turbulent viscosity predicted by the simulation with the One-Equation model is very high in regions of pure shear, especially within glottis. This may be the reason why the simulation with the OE model predicted most of the time the lowest intraglottal velocity. In contrast to this, WALE and AMD subgrid-scale models predicted considerably lower subgrid-scale viscosity in the shear layers at t_N and t_C. The fields computed by the AMD model seem to be similar to fields computed by WALE with spots of gently higher subgrid-scale viscosity at t_N and t_C. The other situation occurs in t_O when the turbulent viscosity predicted by the AMD model is around two times higher than by OE and five times higher than by WALE.

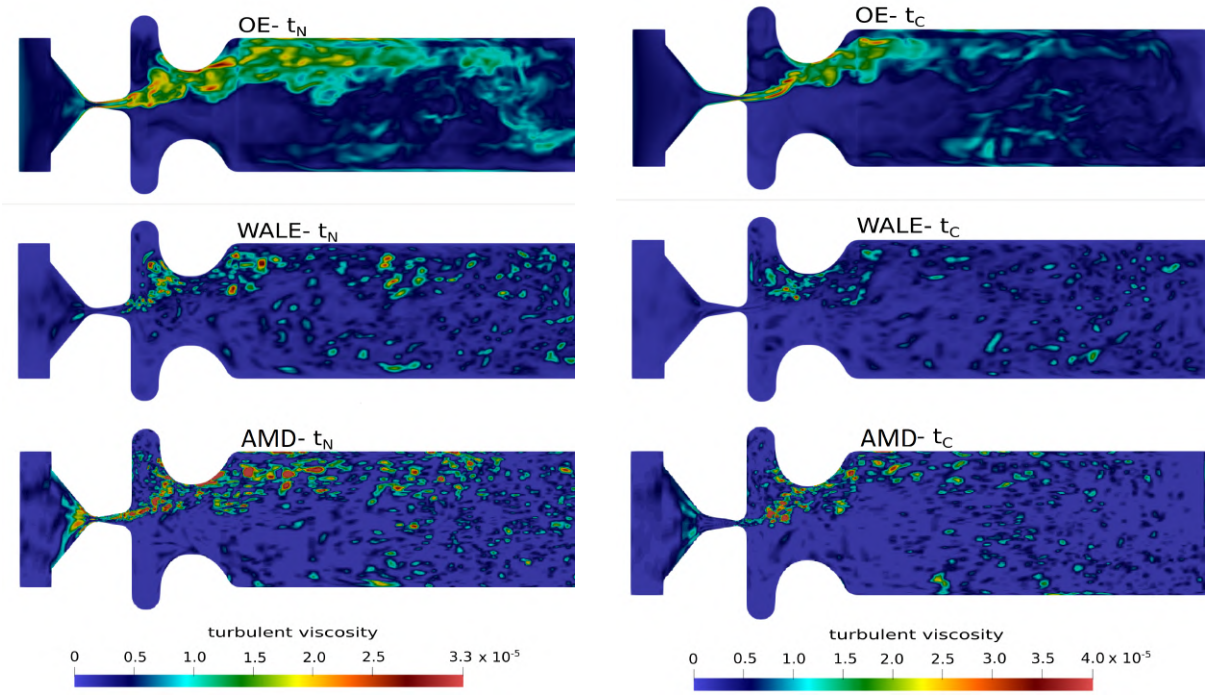

Fig. 2.6: Turbulent viscosity ν_t [$m^2.s^{-1}$] in the mid-coronal plane at t_N (left) and t_C (right).

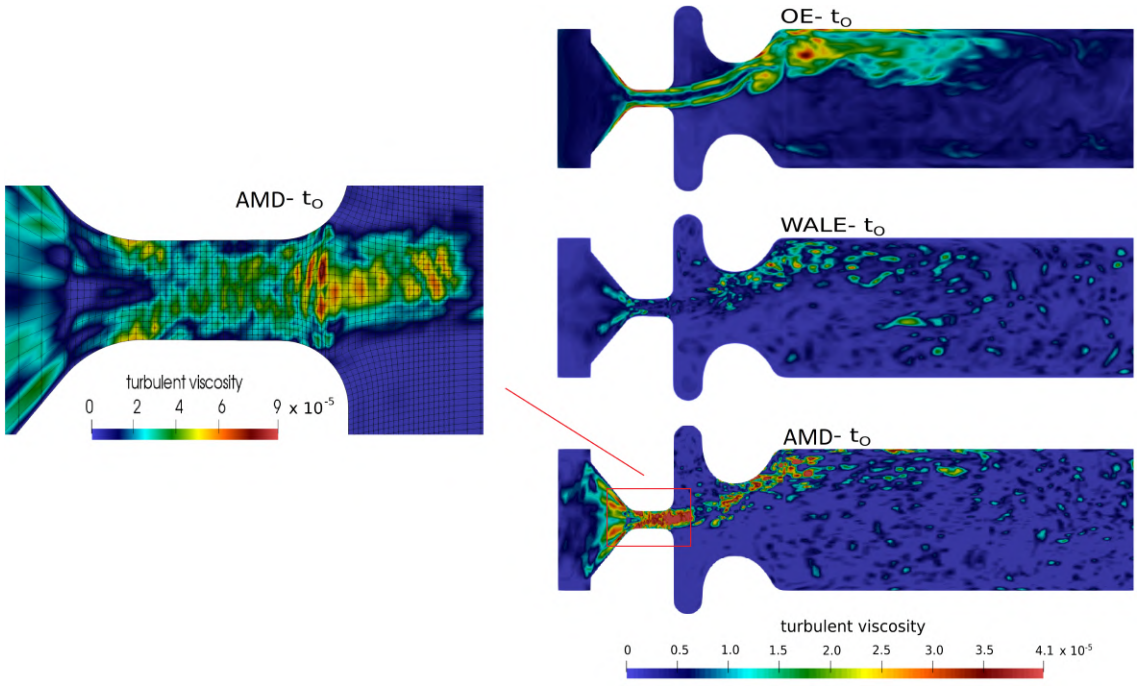

Fig. 2.7: Turbulent viscosity ν_t [$m^2.s^{-1}$] in the mid-coronal plane presented at fully open vocal folds.

Fig. 2.8 shows turbulent viscosity fields in mid-sagittal plane. The simulation with OE predicted twice higher turbulent viscosity located at vicinity of the inferior margin of the vocal folds than others. The narrow barrier of turbulent viscosity at t_N in the case with AMD reduced the flow rate just by 0.8% (1 ml/s of air) compared to WALE.

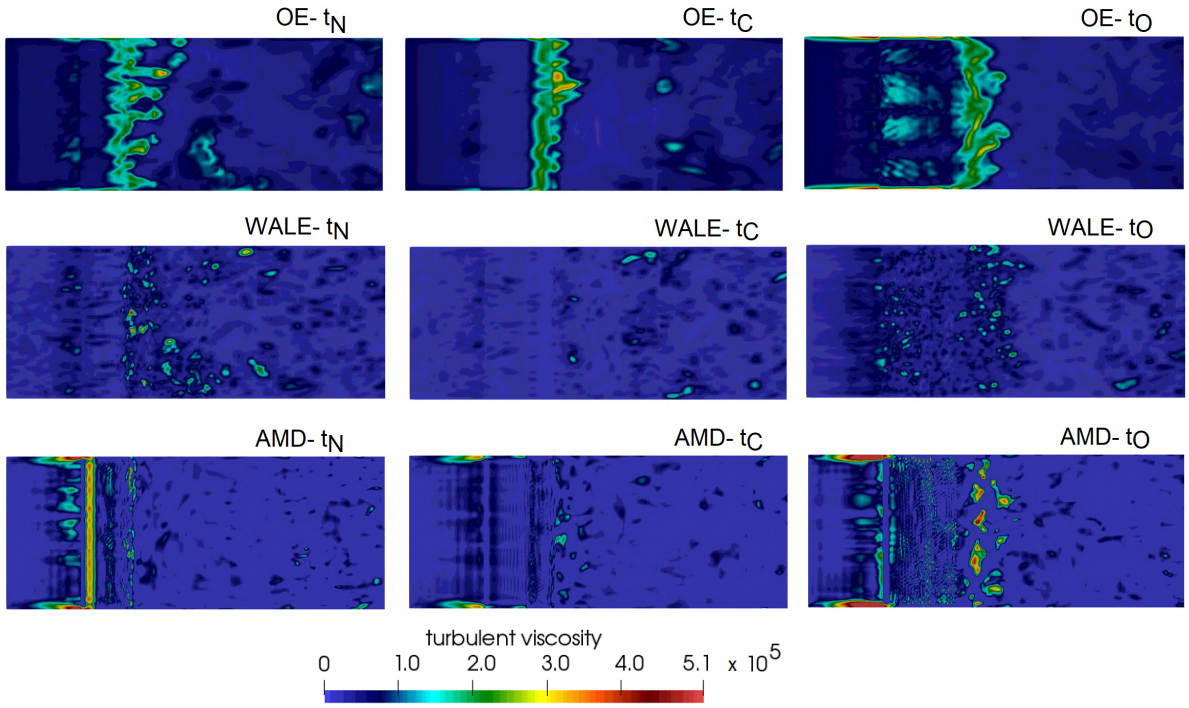

Fig. 2.8: Turbulent viscosity ν_t [$m^2.s^{-1}$] in the mid-sagittal plane.

2.6 Summary of findings

This paragraph summarizes the major findings after performing four CFD simulations of laryngeal flow based on various subgrid-scale models.

- Subgrid-scale turbulence model selection and configuration: The adjustment of dynamic constant in the subgrid-scale turbulence model and damping functions is not needed when the WALE and AMD models are used for the simulation of wall-bounded flows. The models contain a prediction of turbulent viscosity combining the strain rate and rotation rate tensor.

- Benchmark cases: The newly implemented AMD model has been subjected to two tests. The normalized velocity profiles from simulations of turbulent flow within the periodic plane channel were compared with DNS. The AMD model achieved better agreement with the DNS curve than the conventional WALE model. However, the second verification case showed that the AMD model has a tendency to overpredict the mean velocity in the middle of the channel.

- Laryngeal flow rates: The simulation with AMD predicted by 5.1% lower, 11.6% lower and 8.7% higher maximum than the WALE, LAM and OE models, respectively. In the AMD and OE cases, the peak flow rate in the vocal fold

oscillation cycle occurs noticeably sooner than with LAM and WALE subgrid-scale models.

- Velocity fields: High value of the turbulent viscosity has a tendency to reduce the airflow in the glottis and decrease intraglottal velocity. The simulation using the OE model, which is known to overestimate the turbulent viscosity near walls, confirms this statement.

- Vorticity fields: In the glottis was observed a significant reduction of vorticity predicted by AMD compared to WALE and the other models. This finding confirms the expectation that the AMD model is able to stop the production of the scaled velocity gradient energy, and hence the minimum dissipation is kept to a suitable range. This feature leads to the increased estimation of local turbulent viscosity, which smooths the rotation of velocity.

- Turbulent viscosity: The simulation with the AMD model predicted the highest local increase of the turbulent viscosity, identified directly before the glottal constriction and partly on the sagittal walls. The OE model also predicts high turbulent viscosity, expecially in the vicinity of the vocal fold margins and in the shear layer. The AMD model contributed to less turbulence intensity in the glottis.

3 CAA model of wave propagation in vocal tract

Aeroacoustics deals with flow-induced sound generation and wave propagation. Sound generation is caused by the turbulent motion of fluid, periodic varying flow fields, or aerodynamic forces acting on solids. The sources in the case of human phonation are commonly denoted as:

i. A monopole source term due to the motion of vocal folds (the term is zero when the vocal folds are fixed).

ii. A dipole source term due to the unsteady force exerted by the surface of the vocal folds onto the fluid.

iii. A quadrupole sound term due to the unsteady flow inside the vocal tract.

See (Zhao et al., 2002) for more details.

The numerical simulation of aeroacoustic effects can be performed either by using direct simulations or hybrid methods. Direct simulation is based on the compressible Navier-Stokes equations, which capture both the fluid dynamic and acoustic fluctuations. The limitation of this approach is hidden in the computational effort associated with the disparity of scales between the flow and acoustic variables (the small turbulent scales and the large acoustic wavelength during common speech), which can reach several orders of magnitude. To circumvent this problem, hybrid approaches are commonly used, where the flow field and the acoustic field are computed separately (Bae and Moon, 2008; Schoder et al., 2020; Lasota et al., 2021; Valášek, 2021). This work is also based on the hybrid approach.

For simplicity, the overbars $(\bar{\cdot})$ from the LES filtering are dropped in the following paragraphs and equations.

3.1 Aeroacoustic models

In this dissertation is used a hybrid method based on the incompressible flow computation and utilizing a perturbation approach to obtain perturbation equations for the aeroacoustic simulation.

3.1.1 Perturbed Convective Wave Equation (PCWE)

The acoustic perturbation equations form (APE-2) for isothermal and low Mach numbers can be written as a system of three partial differential equations (Hüppe et al., 2014)

$$\frac{\partial \rho'}{\partial t} + \boldsymbol{\nabla} \cdot (\rho' \mathbf{u}_0 + \rho_0 \mathbf{u}^a) = 0, \tag{3.1}$$

$$\rho_0 \frac{\partial \mathbf{u}^a}{\partial t} + \rho_0 \boldsymbol{\nabla} (\mathbf{u}_0 \cdot \mathbf{u}^a) + \boldsymbol{\nabla} p' = \mathbf{0}, \tag{3.2}$$

$$\frac{\partial p^a}{\partial t} - c_0^2 \frac{\partial \rho'}{\partial t} = -\frac{\partial p^{ic}}{\partial t}, \tag{3.3}$$

where the last equation has a source term. Combining (3.1), (3.3) and the equation of state $\rho' = p'/c_0^2$ leads (after some manipulation) to

$$\frac{1}{c_0^2}\left(\frac{\partial p^a}{\partial t} + \mathbf{u}_0 \cdot \boldsymbol{\nabla} p'\right) + \rho_0 \boldsymbol{\nabla} \cdot \mathbf{u}^a = -\frac{1}{c_0^2}\frac{\partial p^{ic}}{\partial t}, \tag{3.4}$$

and employing $p' = p^{ic} + p^a$ the form results in

$$\frac{1}{c_0^2}\left(\frac{\partial p^a}{\partial t} + \mathbf{u}_0 \cdot \boldsymbol{\nabla} p^a\right) + \rho_0 \boldsymbol{\nabla} \cdot \mathbf{u}^a = -\frac{1}{c_0^2}\left(\frac{\partial p^{ic}}{\partial t} + \mathbf{u}_0 \cdot \boldsymbol{\nabla} p^{ic}\right). \tag{3.5}$$

Next, (3.2) and (3.5) are modified. (3.5) is differentiated with respect to time, on (3.2) is taken a divergence, and finally mean flows are neglected; after modifications the equations result in the exact reformulation of APE-2

$$\frac{1}{c_0^2}\frac{\partial^2 p^a}{\partial t^2} - \boldsymbol{\nabla} \cdot \boldsymbol{\nabla} p^a = -\frac{1}{c_0^2}\frac{\partial^2 p^{ic}}{\partial t^2}. \tag{3.6}$$

If the relation $\mathbf{u}^a = -\boldsymbol{\nabla}\psi^a$ is used in (3.2)

$$\rho_0 \frac{\partial(-\nabla\psi^a)}{\partial t} + \rho_0 \nabla(\mathbf{u}_0 \cdot (-\nabla\psi^a)) + \nabla p^a = \mathbf{0}, \tag{3.7}$$

then

$$\nabla\left(\rho_0 \frac{\partial \psi^a}{\partial t} + \rho_0 \mathbf{u}_0 \cdot \nabla\psi^a - p^a\right) = \mathbf{0}. \tag{3.8}$$

The argument of the gradient is a constant, which can be set to zero, and results in the acoustic pressure

$$p^a = \rho_0 \frac{\mathrm{D}\psi^a}{\mathrm{D}t} = \rho_0 \frac{\partial \psi^a}{\partial t} + \rho_0 \mathbf{u}_0 \cdot \nabla\psi^a. \tag{3.9}$$

Now, (3.5) can be rewritten using the substantial derivative to

$$\frac{\mathrm{D}p^a}{\mathrm{D}t} + \rho_0 c_0^2 \boldsymbol{\nabla} \cdot \mathbf{u}^a = -\frac{\mathrm{D}p^{ic}}{\mathrm{D}t}, \tag{3.10}$$

and finally the relation (3.9) is inserted into (3.10), using $\mathbf{u}^a = -\boldsymbol{\nabla}\psi^a$ and multiplied by $1/\rho_0 c_0^2$; a scalar-valued partial differential equation called Perturbed Convective Wave Equation (PCWE) published first by Hüppe et al. (2014) is obtained

$$\frac{1}{c_0^2}\frac{\mathrm{D}^2\psi^a}{\mathrm{D}t^2} - \nabla \cdot \nabla(\psi^a) = -\frac{1}{\rho_0 c_0^2}\frac{\mathrm{D}p^{ic}}{\mathrm{D}t}. \tag{3.11}$$

The vector-valued APE-2 has been reformulated into the scalar PCWE, which can spare computational resources avoiding the vector form. In this dissertation PCWE was used in all cases, while following should be remembered:

- The sound sources are discussed in terms of $\mathrm{D}p^{ic}/\mathrm{D}t$, i.e. in dimension [Pa/s].

- The wave propagation (3.11) contains the factor $-1/(\rho_0 c_0^2) = -1/(1.025 \cdot 343.25^2) = -0.0000087$ ms^2/kg.
- From the solution of equation (3.11), i.e. ψ^a, the acoustic pressure p^a [Pa] is calculated according to (3.9). The convective term $\rho_0 \mathbf{u}_0 \cdot \nabla \psi^a$ contributes only a minor part to the solution, and thus $p^a = \rho_0 \partial \psi^a / \partial t$ is computed.

Benefits of PCWE are evident: faster computation with a scalar unknown, lower memory requirements compared to the APE-x forms, includes convection inside the wave operator and solves the acoustic quantity compared to Lighthill's analogy (Lighthill, 1952).

3.2 Geometry and mesh

Fig. 3.1 illustrates the geometry used for aeroacoustic simulations, where from the left side are: the PML layer at inlet (dark green), larynx (red), vocal tract (purple) and the radiation zone protected by PML (green hollow cube). PML (Perfectly matched layer) is a technique published first by Berenger (1994). The original method was modified by Kaltenbacher et al. (2013) by adding damping layers to guarantee that no wave reflections occur at boundaries.

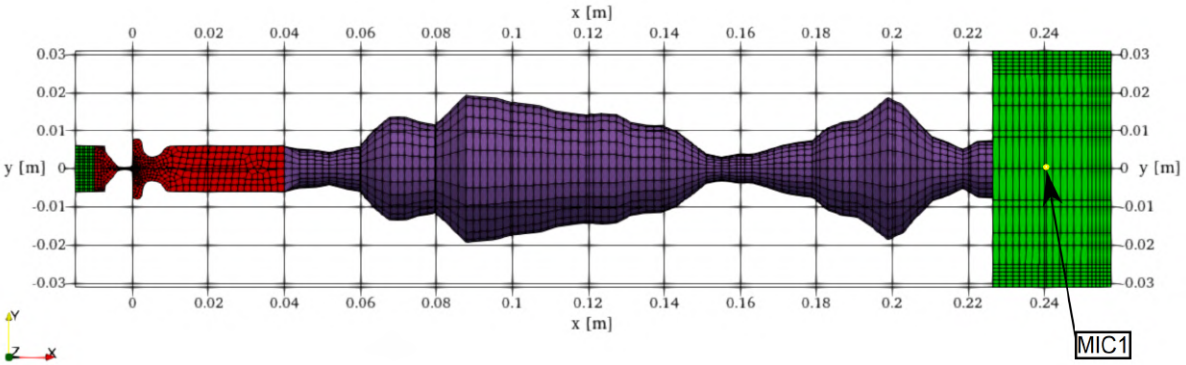

Fig. 3.1: Geometry and mesh representation for the aeroacoustic simulation. This vocal tract is in the shape for vowel /u/.

In this work five geometric models of vocal tracts were created. The models correspond to vowels /u, i, ɑ, o, æ/. Tab. 3.1 lists the lengths of vocal tracts of five English vowels.

Tab. 3.1: List of used vocal tracts (VT).

Phonetic symbol	**VT length** [m]	**Nb. of segments**	**Example of use**
/u/	0.1825	46	who [hu:]
/i/	0.1667	42	heed [hi:d]
/ɑ/	0.1746	44	lock [lɑk]
/o/	0.1746	44	rock [rok]
/æ/	0.1667	42	have [hæv]

The shape parameters of vocal tracts came from the study provided by Story et al. (1996). The three-dimensional vocal tracts used in CAA simulations are shown in Figs. 3.2-3.4 and were built in Gmsh.

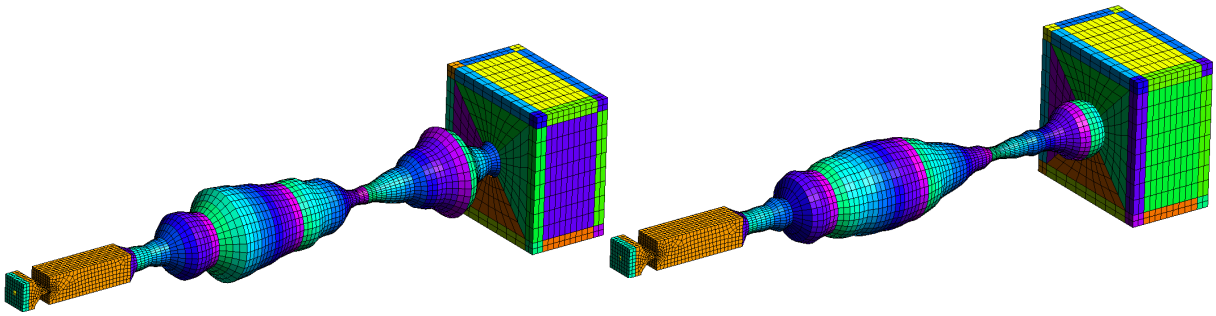

Fig. 3.2: Visualization of the acoustic mesh for /u/ (left) and /i/ (right).

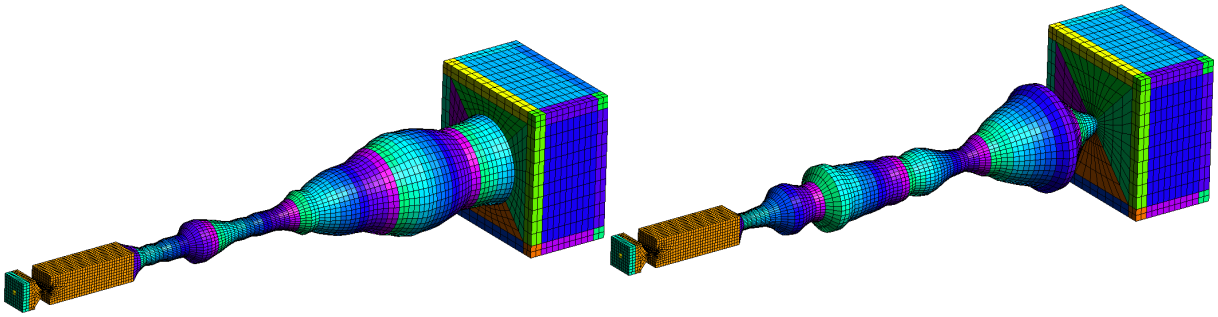

Fig. 3.3: Visualization of the acoustic mesh for /ɑ/ (left) and /o/ (right).

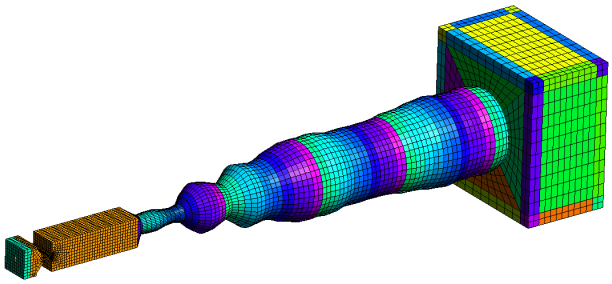

Fig. 3.4: Visualization of the acoustic mesh for /æ/.

The number of elements and nodes is listed in Tab. 3.2.

Tab. 3.2: Five computational meshes for the aeroacoustic simulation.

vowel	**elements**	**nodes**
/u/	11,736	14,689
/i/	11,256	14,077
/ɑ/	18,818	23,051
/o/	18,818	23,051
/æ/	18,484	22,567

3.3 Boundary conditions

The partial differential equation (3.11) for the acoustic potential ψ^a, which will be solved numerically in the acoustic domain, is equipped with zero initial conditions and boundary condition

$$\boldsymbol{\nabla}\psi^a \cdot \mathbf{n} = 0, \tag{3.12}$$

where $\mathbf{n}$ is the outward unit normal. The boundary condition can be interpreted as a perfect reflection of a sound wave from a barrier, also the condition is called "sound hard". In these computations, the sound hard condition is applied at all boundaries except the inflow and outflow, where PML is used.

3.4 Discretization and numerical solution

An open source 3D finite element mesh generator Gmsh (available online: https://gmsh.info/) was used to build the computational mesh. The element length Δl^a of the acoustic mesh and time step Δt^a for the aeroacoustic simulation are given by estimations (Hüppe, 2012)

$$\Delta l^a \leq \frac{c_0}{20 f_{\max}} = 3.43 \text{ mm}, \quad \Delta t^a \leq \frac{1}{20 f_{\max}} = 1 \cdot 10^{-5} \text{ s}, \tag{3.13}$$

assuming that 20 linear finite elements per one acoustic wavelength are sufficient. In this case, the spatial discretization is limited by 3.43 mm and time step by $1 \cdot 10^{-5}$ s in order to resolve properly acoustic frequencies up to $f_{\max} = 5$ kHz. If the condition is not satisfied, then the acoustic results are affected by high dissipation and dispersion (Kaltenbacher, 2018). The acoustic material properties in simulations are defined by the density $\rho = 1.11703$ kg.m^{-3}, the bulk modulus $K = 0.1156$ MPa and the speed of sound $c_0 = 343.25$ m.s^{-1}.

The numerical solution (workflow) can be separated into three steps:

- The unsteady flow field in the larynx is computed in OpenFOAM on a fine CFD mesh over 20 periods of vocal fold oscillation.
- The aeroacoustic sources in the larynx are computed by OpenCFS, and conservatively interpolated on the coarse CAA mesh.
- In the last step, the wave propagation is simulated by OpenCFS on the coarse CAA mesh.

The computational time needed for one CAA simulation is much lower than for one CFD simulation, about five hours on a single CPU core compared to 34 days on 20 cores. But it should be noted that five CAA simulations have been computed on top of each of the CFD simulations. Altogether, four CFD simulations and 20 CAA simulations have been performed in this work. The conservative interpolation of the sound source from the very fine (2.2M) CFD mesh to the coarser (11k-18k) CAA mesh was performed by the cfsdat tool (part of the OpenCFS). The work of Schoder et al. (2020) contains an overview of the conservative strategies, granting a reduction of the simulation time.

3.5 CAA results

3.5.1 Visualization of sound sources in the time domain

The distribution of the aeroacoustic sources in the computational domain covering the larynx varies throughout the vocal fold oscillation period. Fig. 3.5 shows the aeroacoustic source field while the vocal folds are in the closed-divergent position. The jet is surrounded by spots of strong positive and negative acoustic sources related to turbulent eddies created from shear layers of the jet.

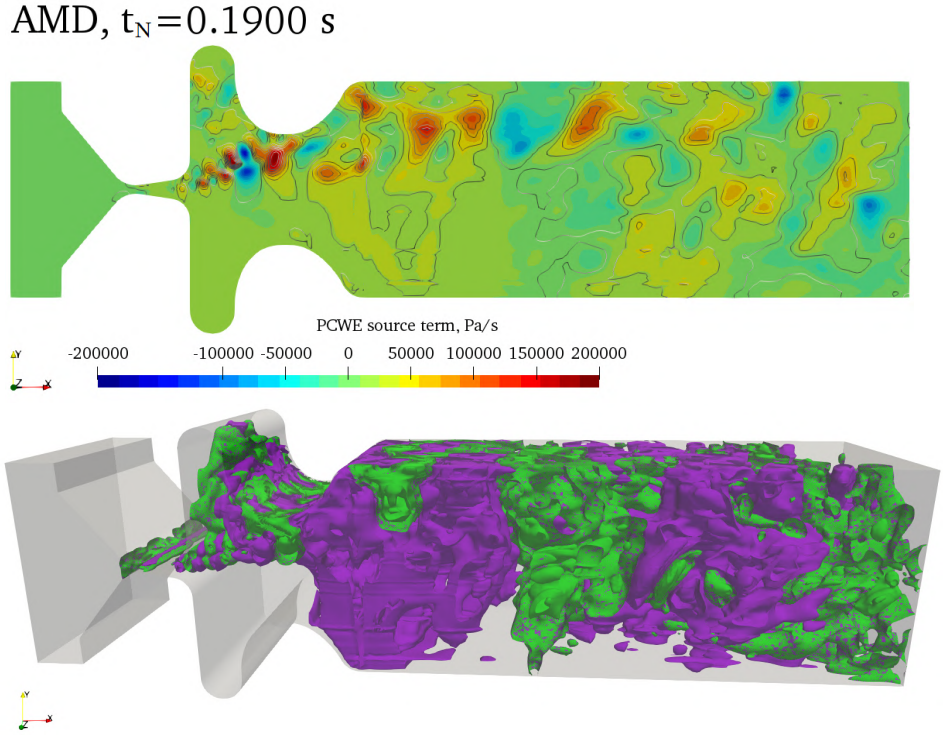

Fig. 3.5: Aeroacoustic source term ($\mathrm{D}p^{ic}/\mathrm{D}t$) from (3.11) at closed-divergent vocal folds positions during phonation. Twenty iso-surfaces in the range $\pm 2 \cdot 10^5$ Pa/s are shown (positive-purple ones, negative-green ones).

3.5.2 Visualization of sound sources in the frequency domain

The conversion from the time to frequency domain was made by the field Fast Fourier Transform (field FFT), which brings useful insight into the spatial distribution of the aeroacoustic sources at distinct frequencies related somehow to human phonation.

Fig. 3.6 shows the 3D spatial distribution of sound sources in the supraglottal volume at $f = 1000$ Hz and $f = 1235$ Hz. At the non-harmonic frequency the acoustic sources are distributed further downstream. The integrity of sound sources can be observed, along with several local sound spots at the superior (trailing) edge of vocal folds.

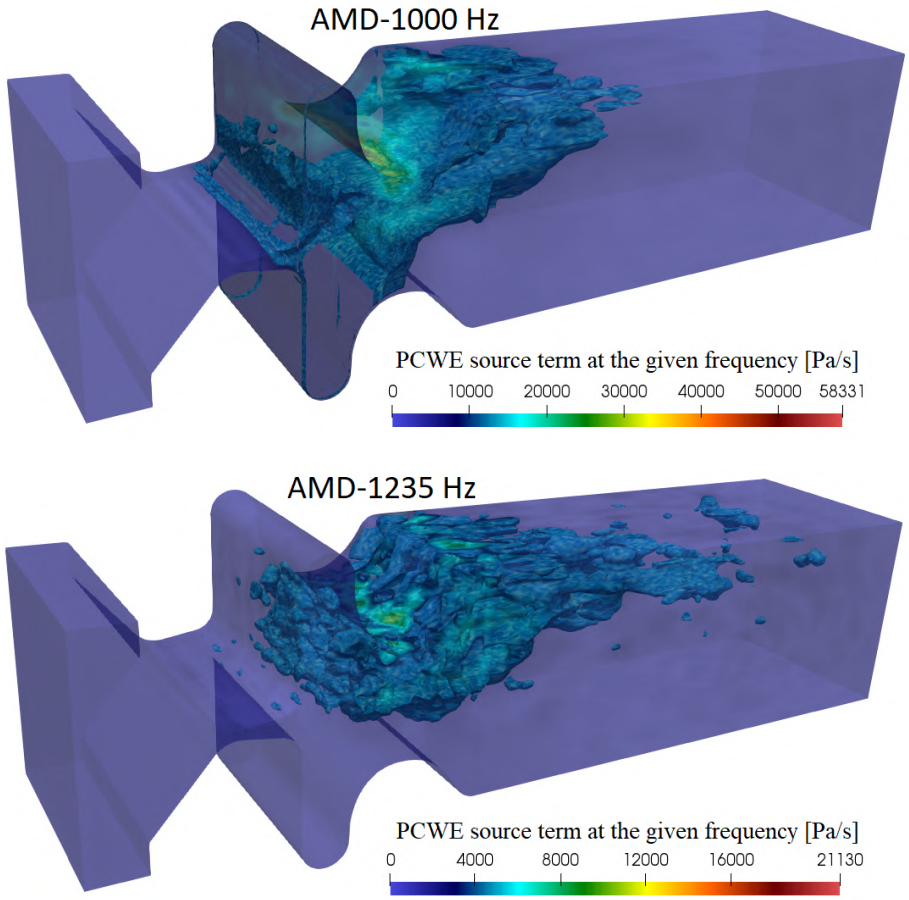

Fig. 3.6: 3D spatial distribution of the PCWE source term at the harmonic frequency f=1000 Hz and the non-harmonic frequency f = 1235 Hz.

3.5.3 Wave propagation in the frequency domain

This section deals with frequency spectra. This kind of analysis can highlight fundamental, harmonic and non-harmonic frequencies, accompanied by background noise. The FFT analyses were performed on the signal of 20 periods of the vocal fold oscillation (1 period = 10 ms = 1000 samples), and thus the frequency resolution is $\Delta f = 5$ Hz. The spectra will be analysed vowel by vowel.

Vowel /u/. Fig. 3.7 shows aeroacoustic spectrum based on the CFD simulation with different subgrid-scale models. SPL at fundamental frequency $f_o = 100$ Hz and higher harmonics $f_1 = 200$ Hz, $f_2 = 300$ Hz and so forth, are well visible, but SPL at f_o is lower than at f_1 and f_2. Unfortunately, this trend is in contrast with the acoustic theory, meaning the oscillation of vocal folds is simultaneously the dominant frequency in the spectrum. Scientific groups (Falk et al., 2021; Schoder et al., 2020) report the same unbalance with the first harmonic L_{f_1} higher than L_{f_o}. The second formant computed by the simulation with AMD is higher by 22% compared to the case with WALE. At the third formant, on the contrary, WALE is higher by 28% than AMD. This trend occurs only for vowels /u, ɑ/, even though the vocal tracts for /u, ɑ/ have very different shapes (see Fig. 3.4).

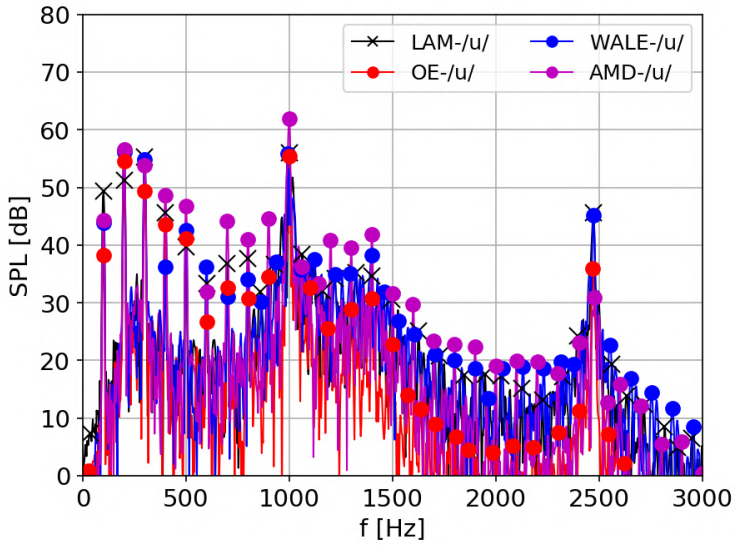

Fig. 3.7: Acoustic sound spectra from the numerical simulation of vocalization of /u/ at monitoring point MIC 1.

Vowel /i/. Fig. 3.8 shows the second aeroacoustic spectrum. The simulations with OE performed on vocal tracts /u, i/ predict the lowest SPL at the fundamental frequencies.

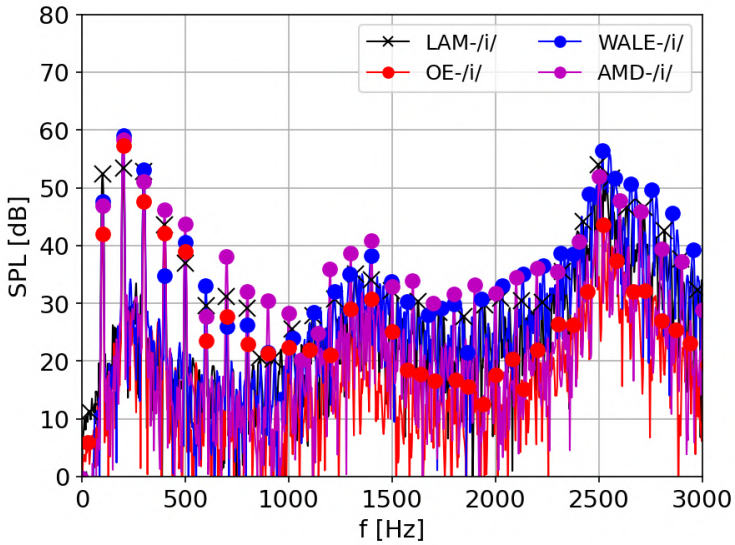

Fig. 3.8: Acoustic sound spectra from the numerical simulation of vocalization /i/ at monitoring point MIC 1.

Vowel /ɑ/. Fig. 3.9 shows that SPLs at fundamental frequency remain at the same level for all models. This happened only twice, in cases /ɑ, æ/ for open and mid-open vowels, when the tongue is pressed down most. The close distance between formants $F_1 - F_2$ is typical for vowels /u, ɑ, o/, but in the simulation of /ɑ/ the second formant around 1300 Hz was not detected. However, in the case of AMD, it appears that the second formant may be found. On the other hand, the third formant is clearly visible and presents the same behavior as in /u/, i.e. a 9-13 dB lower value of AMD compared to WALE and LAM.

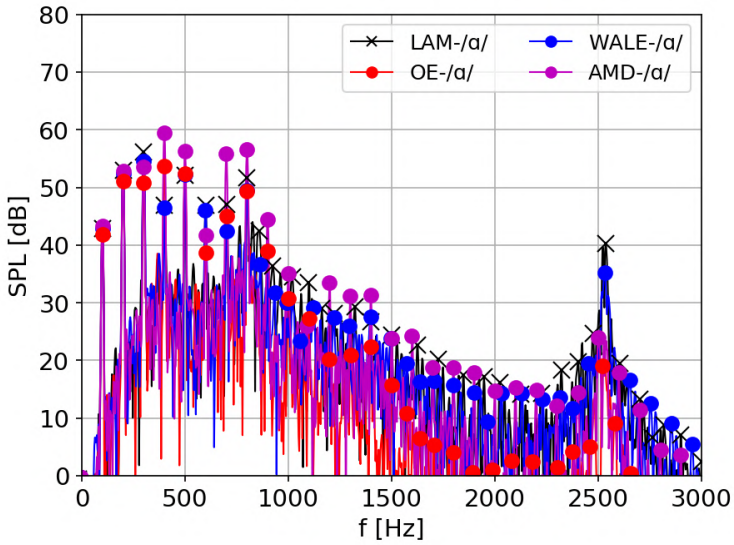

Fig. 3.9: Acoustic sound spectra from the numerical simulation of vocalization of /ɑ/ at monitoring point MIC 1.

Vowel /o/. Fig. 3.10 shows the aeroacoustic spectrum with the widest passage of the throat (7.25 cm^2) during phonation. The simulation with the AMD model predicted the first formant around 900 Hz and SPL around 64 dB. At 30 cm, the value would reach 34 dB.

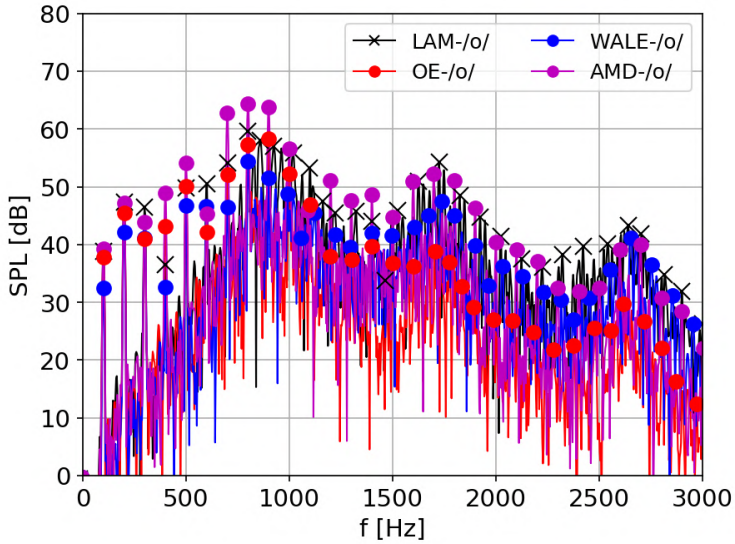

Fig. 3.10: Acoustic sound spectra from the numerical simulation of vocalization of /o/ at monitoring point MIC 1.

Vowel /æ/. Fig. 3.11 shows the aeroacoustic spectrum for the vocal tract /æ/, which transfers most acoustic energy – 70 dB with the AMD model, 66 dB with the WALE model. The first formant predicted by AMD is by 14 dB higher than the formant predicted by the WALE model. The formants in the high-frequency bandwidth are on the same level for AMD and WALE. For all vowels except /æ/, at 600 Hz was detected a significant drop in SPL.

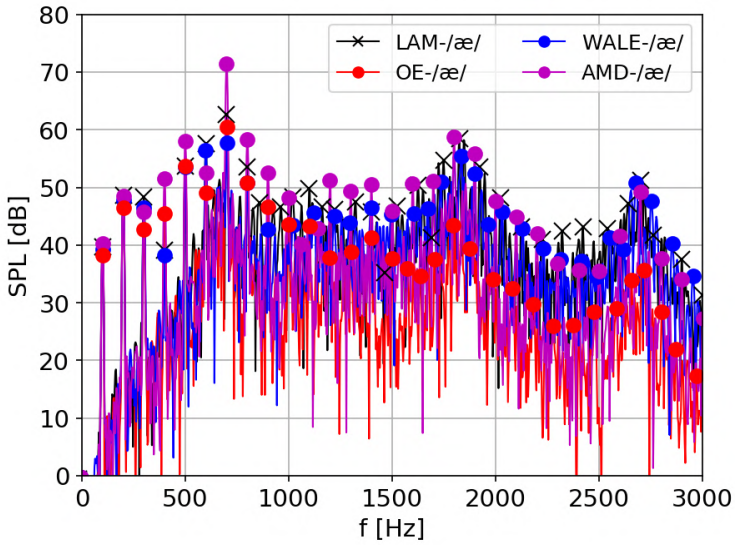

Fig. 3.11: Acoustic sound spectra from the numerical simulation of vocalization of /æ/.

3.6 Summary of findings

Analysis of the CAA simulations leads to the following important conclusions:

- For all vowels, the results of aeroacoustic simulations based on the AMD model have strongest SPL of higher harmonic frequencies up to about 2000 Hz. For frequencies between 2000-3000 Hz, the strongest harmonics are predicted by the WALE model.
- For all vowels, the usage of the AMD model leads to the stronger second formant, whereas the WALE model results in the stronger third formant.
- For all vowels, SPL at 100 Hz was lower than at higher harmonic frequencies. In the case with close-front and close-back vowels this might be an effect of the first formant, but in cases with mid/open and open vowels, when the first formant is far.
- Simulations of phonation including vowels /ɑ, æ/ computed higher SPL compared to vowels /u, i, o/. This could be explained by greater vocal tract passage before lips.
- The subgrid-scale model did not have any influence on the location of the formant frequencies.

4 Conclusion

Large-eddy simulations of laryngeal incompressible flow with no subgrid-scale model (LAM) and with various of subgrid-scale models were performed, namely: One-Equation (OE), Wall-Adaptive Local-Eddy viscosity (WALE) and the newly implemented Anisotropic Minimum-Dissipation (AMD) (2.23) model. The AMD model was tested on benchmark cases prior to use on the laryngeal flow.

CAA simulations of the aeroacoustic sources and wave propagation during human phonation of five vowels /u, i, ɑ, o, æ/ were performed. The simulations were based on the hybrid approach using decomposition of the flow variables. The perturbed convective wave equation (3.11) was used in all cases.

Numerical results obtained from CFD and CAA simulations were discussed separately in summaries of findings (Chaps. 3.6, 2.6). The concluding assessment regarding the usage of SGS models in numerical modelling of human phonation can be formulated as follows: The OE model overpredicts the turbulent viscosity in regions where shear is dominant, i.e. in the boundary layer adjacent to the vocal folds and in the shear layers of the glottal jet (Figs. 2.8, 2.7, 2.6). The difference in glottal flow rate among the simulations is clearly induced by the subgrid-scale model, which adds the turbulent viscosity to the molecular viscosity of air and hinders the airflow in the glottis (Fig. 2.2, Tab. 2.4). The WALE model produced zero eddy viscosity in cases of pure shear flow (Figs. 2.8, 2.7, 2.6), and hence the flow simulation with WALE predicted by 5% higher maximum transglottal flow rate than AMD (Fig. 2.2, Tab. 2.4). Despite of this fact, the phonation simulation based on the AMD model transferred more energy in terms of total sound pressure level than WALE for all vowels except the front-close vowel /i/.

The WALE model, which is known to handle turbulent viscosity at the near-wall and high-shear regions more precisely than the OE model, resulted in higher SPLs than OE in all cases except the close-back vowel /u/. The OE model gives acceptable results in general, but peaks of frequency formants are hardly visible and weaker compared to the WALE or AMD model. The WALE model amplified third formants in high-frequency bandwidth most of all the models (Figs. 3.7-3.11). Hovewer, the third formant is not crucial for vowel characterization.

The AMD model seems to be a very promising successor to the WALE model in modelling laryngeal flow, since the AMD model resulted in significantly higher harmonic frequencies up to the second formant for all studied cardinal vowels (Figs. 3.7-3.11). This finding could be related to known features of the AMD model: consistency with the exact subgrid-scale stress tensor τ_{ij}, no requirements on the approximation of the filter width Δ and usability on an anisotropic mesh. This thesis represents the first application of the AMD model in the field of human phonation.

References

M. Agarwal, R. Scherer, and H. Hollien. The false vocal folds: shape and size in frontal view during phonation based on laminagraphic tracings. *Journal of Voice*, 17(2):97–113, June 2003. DOI 10.1016/S0892-1997(03)00012-2.

Y. Bae and Y. J. Moon. Computation of phonation aeroacoustics by an ins/pce splitting method. *Computers & fluids*, 37(10):1332–1343, 2008. DOI 10.1016/j.compfluid.2007.12.002.

J.-P. Berenger. A perfectly matched layer for the absorption of electromagnetic waves. *Journal of computational physics*, 114(2):185–200, 1994. DOI 10.1006/jcph.1994.1159.

A. Clark, H. Ferziger, and C. Reynolds. Evaluation of subgrid-scale models using an accurately simulated turbulent flow. *Journal of fluid mechanics*, 91(1):1–16, 1979. DOI 10.1017/s002211207900001x.

B. Erath and M. Plesniak. An investigation of asymmetric flow features in a scaled-up driven model of the human vocal folds. *Experiments in Fluids*, 49(1):131–146, 2010. DOI 10.1007/s00348-009-0809-0.

S. Falk, S. Kniesburges, S. Schoder, B. Jakubaß, P. Maurerlehner, M. Echternach, M. Kaltenbacher, and M. Döllinger. 3d-fv-fe aeroacoustic larynx model for investigation of functional based voice disorders. *Frontiers in Physiology*, 12:226, 2021. ISSN 1664-042X. DOI 10.3389/fphys.2021.616985.

H. Ferziger. Direct and large eddy simulation of turbulence. *Numerical methods in fluid mechanics*, 16:53–73, 1998. DOI 10.1299/kikaib.66.651$_2$754.

C. A. Fletcher. Fluid dynamics: The governing equations. In *Computational Techniques for Fluid Dynamics 2*, pages 1–46. Springer: Berlin/Heidelberg, 1991. DOI 10.1007/978-3-642-58239-4$_1$.

A. Hüppe, J. Grabinger, M. Kaltenbacher, A. Reppenhagen, G. Dutzler, and W. Kühnel. A non-conforming finite element method for computational aeroacoustics in rotating systems. In *20th AIAA/CEAS Aeroacoustics Conference*, page 2739, 2014. DOI 10.2514/6.2014-2739.

A. Hüppe. *Spectral Finite Elements for Acoustic Field Computation*. PhD thesis, Alps-Adriatic University of Klagenfurt, 2012.

H. Jasak. *Error analysis and estimation for the finite volume method with applications to fluid flows*. PhD thesis, 1996.

B. Kaltenbacher, M. Kaltenbacher, and I. Sim. A modified and stable version of a perfectly matched layer technique for the 3-d second order wave equation in time domain with an application to aeroacoustics. *Journal of computational physics*, 235:407–422, 2013. DOI 10.1016/j.jcp.2012.10.016.

M. Kaltenbacher. *Computational Acoustics*. Springer, 2018. ISBN 978-3-319-59038-7. DOI 10.1007/978-3-319-59038-7.

M. Lasota, P. Šidlof, M. Kaltenbacher, and S. Schoder. Impact of the sub-grid scale turbulence model in aeroacoustic simulation of human voice. *Applied Sciences*, 11(4): 1970, Feb. 2021. DOI 10.3390/app11041970.

D. R. Launchbury. *Unsteady turbulent flow modelling and applications*. Springer: Berlin/Heidelberg, 2016.

A. Leonard. Energy cascade in large-eddy simulations of turbulent fluid flows. In *Advances in geophysics*, volume 18, pages 237–248. Elsevier: Amsterdam, The Netherlands, 1975. DOI 10.1016/S0065-2687(08)60464-1.

M. Lesieur, O. Métais, and P. Comte. *Large-eddy simulations of turbulence*. Cambridge University Press: Cambridge, UK, 2005.

M. J. Lighthill. On sound generated aerodynamically. I. General theory. In *Proceedings of the Royal Society of London A: Mathematical, Physical and Engineering Sciences*, volume 211, pages 564–587. The Royal Society, 1952. DOI 10.1098/rspa.1952.0060.

A. Lodermeyer, S. Becker, M. Döllinger, and S. Kniesburges. Phase-locked flow field analysis in a synthetic human larynx model. *Experiments in Fluids*, 56(4):1–13, 2015. DOI 10.1007/s00348-015-1942-6.

W. Rozema, H. J. Bae, P. Moin, and R. Verstappen. Minimum-dissipation models for large-eddy simulation. *Physics of Fluids*, 27(8):085107, 2015. DOI 10.1063/1.4928700.

R. Scherer, D. Shinwari, J. De Witt, C. Zhang, R. Kucinschi, and A. Afjeh. Intraglottal pressure profiles for a symmetric and oblique glottis with a divergence angle of 10 degrees. *The Journal of the Acoustical Society of America*, 109(4):1616–1630, 2001. DOI 10.1121/1.1333420.

S. Schoder, M. Weitz, P. Maurerlehner, A. Hauser, S. Falk, S. Kniesburges, M. Döllinger, and M. Kaltenbacher. Hybrid aeroacoustic approach for the efficient numerical simulation of human phonation. *The Journal of the Acoustical Society of America*, 147(2):1179–1194, 2020. DOI 10.1121/10.0000785.

P. Šidlof, S. Zörner, and A. Hüppe. A hybrid approach to the computational aeroacoustics of human voice production. *Biomechanics and modeling in mechanobiology*, 14(3):473–488, 2015. DOI 10.1007/s10237-014-0617-1.

B. H. Story, I. R. Titze, and E. A. Hoffman. Vocal tract area functions from magnetic resonance imaging. *The Journal of the Acoustical Society of America*, 100(1):537–554, 1996. DOI 10.1121/1.415960.

I. R. Titze. *Principles of Voice Production*. Prentice Hall: Englewood Cliffs, NJ, USA, 1994.

J. Valášek. *Numerical Simulation of Fluid-Structure-Acoustic Interaction in Human Phonation*. PhD thesis, Czech Technical University in Prague, 2021.

R. Verstappen. When does eddy viscosity damp subfilter scales sufficiently? *Journal of Scientific Computing*, 49(1):94–110, 2011. DOI 10.1007/978-94-007-0231-8_38.

H. K. Versteeg and W. Malalasekera. *An introduction to computational fluid dynamics: the finite volume method*. Pearson Education: London, UK, 2007.

A. Vreman. An eddy-viscosity subgrid-scale model for turbulent shear flow: Algebraic theory and applications. *Physics of fluids*, 16(10):3670–3681, 2004. DOI 10.1063/1.1785131.

B. Vreman. *Direct and large-eddy simulation of the compressible mixing layer*. PhD thesis, Holland: University of Twente, 1995.

C. A. Vreugdenhil and J. R. Taylor. Large-eddy simulations of stratified plane couette flow using the anisotropic minimum-dissipation model. *Physics of Fluids*, 30(8):085104, 2018. DOI 10.1063/1.5037039.

A.-P. Zahiri and E. Roohi. Anisotropic minimum-dissipation (AMD) subgrid-scale model implemented in openfoam: verification and assessment in single-phase and multi-phase flows. *Computers & Fluids*, 180:190–205, 2019. DOI 10.1016/j.compfluid.2018.12.011.

W. Zhao, C. Zhang, S. H. Frankel, and L. Mongeau. Computational aeroacoustics of phonation, part i: Computational methods and sound generation mechanisms. *The Journal of the Acoustical Society of America*, 112(5):2134–2146, 2002. DOI 10.1121/1.1506693.

S. Zörner, P. Šidlof, A. Hüppe, and M. Kaltenbacher. Flow and acoustic effects in the larynx for varying geometries. *Acta Acustica united with Acustica*, 102(2):257–267, 2016. DOI 10.3813/AAA.918942.